Two Novel PET Image Restoration Methods Guided by PET-MR Kernels: Application to Brain Imaging

Marzieh S. Tahaei

McConnell Brain Imaging Centre, Montreal Neurological Institute, Montreal, Canada and

*Dept. of Biomedical Engineering, McGill University, Montreal, Canada**

Andrew J. Reader

Dept. of Biomedical Engineering, Division of

Imaging Sciences and Biomedical Engineering,

King's College London, St. Thomas' Hospital, London, UK

D. Louis Collins

McConnell Brain Imaging Centre, Montreal Neurological Institute, Montreal, Canada

Dept. of Biomedical Engineering, McGill University, Montreal, Canada

Abstract

Purpose: Post-reconstruction PET image restoration methods that take advantage of available anatomical information can play an important role in accurate quantification of PET images. However, when using anatomical information, the resulting PET image may lose resolution in certain regions where the anatomy does not agree with the change in functional activity. In this work this problem is addressed by using both MR and filtered PET images to guide the denoising process.

Methods: In this work, two novel post-reconstruction methods for restoring PET images using the subject's registered T1-weighted MR image, are proposed. The first method is based on a representation of the image using basis functions extracted from T1-weighted MR and filtered PET image. The coefficients for these basis functions are estimated using a sparsity-penalized least squares objective function. The second method is a non-iterative fast method that uses guided kernel filtering in combination with twicing to restore the noisy PET image. When applied after conventional PVE correction, these methods can be considered as voxel-based MR-guided partial volume effect (PVE) correction methods.

Results: Using simulation analyses of [^{18}F]FDG PET images of the brain with lesions, the proposed methods are compared to other denoising methods through different figures-of-merit. The results show promising improvements in image quality as well as reduction in bias and variance of the lesions. We also show the application of the second method on real [^{18}F]FDG data.

Conclusion: Two methods for restoring PET images were proposed. The methods were evaluated on simulation and real brain images. Most MR-guided PVE correction methods are only based on segmented T1-weighted images and their accuracy is very sensitive to segmentation errors, especially in regions of abnormalities and lesions. However, both proposed methods can use the T1-weighted image without segmentation. The simplicity and the very low computational cost of the second method make it suitable for clinical applications and large data studies. The proposed methods can be naturally extended to PVE correction and denoising of other functional modalities using corresponding anatomical information.

Key words: PET, MR, denoising, post-reconstruction, sparsity, PVE correction, basis functions, twicing, multi-centric studies, brain imaging

* marzieh.tahaei@mail.mcgill.ca

I. INTRODUCTION

PET imaging plays an important role in the diagnosis, treatment and drug development for different neurological disorders. In addition, using the growing variety of radiotracers, quantitative PET imaging is now considered as a powerful and unique tool for understanding the human brain in health and disease.

Two of the sources of error in quantification of PET images include poor signal-to-noise ratio (SNR) and low spatial resolution. Low SNR is mainly due to the low number of counts imposed by constraints on administrated activity dose, combined with limited scanner sensitivity. SNR is also affected by the acquisition time and the type of radiotracer [7, 25, 36]. The partial volume effect (PVE) is due to positron range, photon-non-colinearity, limited scanner spatial resolution, tissue fraction effects and the reconstruction process [35].

PET images reconstructed using conventional algorithms suffer from increasing amounts of noise with increasing iterations [3]. In practice noise is usually minimized by the early termination of the reconstruction algorithm or by applying Gaussian post-smoothing, which leads to further loss of resolution in the resulting images. Two approaches have been considered to address this issue: one is to use sophisticated reconstruction algorithms which incorporate regularization to reduce the noise in the resulting image [2, 14, 30, 32, 37], and the other is to apply post-reconstruction methods on PET images reconstructed using conventional algorithms [6, 41].

Despite a vast body of research to develop new regularization methods that reduce the noise within reconstruction, most of these advances have not been translated into practice. One reason for the lack of use of these methods in practice is that the measurement data format in many of the current scanners are proprietary and hence only the software provided by the scanner manufacturer can be used to reconstruct images [39]. Therefore, applying a more sophisticated reconstruction algorithm on the raw measurement data obtained from the scanner may not be feasible. In such cases, state-of-the-art post-reconstruction denoising methods can be used to reduce the noise in reconstructed PET images while preserving the resolution.

Over the past several years, advances in computing infrastructure and neuroimaging technologies have led to growth in large data repositories of research and clinical PET images. Using post-reconstruction methods for larger data sets of PET images is of great interest

for several reasons: i) post reconstruction methods can be applied to reconstructed images in large multi-centric studies for which raw measurement data is not available; ii) in order to improve inter-centre consistency, in many multi-centres studies, centres are required to provide images reconstructed using a common, off the shelf reconstruction algorithm (e.g., the ordered subsets expectation maximization algorithm) [19]. Therefore, the noise in these images can only be reduced using a post-reconstruction method. iii) Computational complexity of the post-reconstruction methods is usually much lower than the integration of noise reduction techniques with reconstruction methods.

Many clinical and research PET acquisitions are accompanied by MR images of the same subject and methods that leverage the detailed anatomical information in MR images for PET image restoration (i.e., for PVE correction and denoising) are interesting. The motivation for using MR images for this purpose is that similar MR intensities correspond to similar tissues, and these tissues have a tendency to have similar functions. In fact, many PVE correction methods have used the subject's co-registered and segmented MR to reduce the PVE in the resulting images [4, 16, 28, 34].

In addition to PVE correction, anatomical information has been previously used in denoising PET images [8, 41, 43]. One important challenge in using anatomical images as a guide image for denoising PET images is that the latter may suffer from degraded resolution in regions where the anatomy does not agree with the functional activity in the image. For example a hot spot in the functional image that does not have an anatomical homologue may lose boundary information in the denoised image when using anatomy-constrained methods. This work tries to address these issues by proposing two post-reconstruction frameworks to incorporate both the subject's T1-weighted MR image and the median-filtered PET images in guiding the image denoising process. In the first method, two kernel matrices, one extracted from the MR image and the other extracted from the median-filtered PET image are used as basis functions for PET image re-parameterization. An algorithm to estimate the coefficients of these basis functions is proposed. In order to avoid memory problems due to the large size of the kernel matrix for each 3D image, an implicit matrix-vector multiplication is performed using an operation similar to filtering.

While this method has a rigid mathematical framework, its iterative nature can lead to an excessive computational cost. Therefore, in order to improve the speed of the image denoising, a second very fast non-iterative method for denoising PET images is presented.

This heuristic method is composed of two simple steps. In the first step, the subject's registered MR image is used as the guide image for denoising the PET image. In the second step, the median-filtered PET image is used as the guide image to denoise the residual. The denoised residual is then added to the denoised image from the first step to recover signals specific to the PET image. We also show that these methods, when applied after a conventional deblurring algorithm, can restore the PET image by reducing the noise as well as PVE.

II. METHODOLOGY

In this section a detailed description of the proposed methods is given. Hereafter in the paper, bold capital letters are used to indicate matrices, bold lower-case letters represent column vectors and non-bold letters denote scalar values. Table I summarises the symbols and abbreviations used throughout this paper.

Let $\mathbf{y} \in \mathbb{R}^I$ be a vector of size I representing the voxles of the noisy reconstructed image. The goal is to devise a restoration algorithm to obtain an estimate of the true image $\mathbf{x}$ from $\mathbf{y}$. Let us call this estimate $\hat{\mathbf{x}}$.

A. Guided kernel means (GKM)

In 3D filtering, the estimate of a voxel value $\hat{x}_i$ in the restored image is obtained by a weighted average of other voxels in the image.

The weight associated with voxel y_j in this average is proportional to the similarity of the voxel y_i to y_j as indicated by $k_{i,j}$.

$$\hat{x_i} = \frac{1}{\sum_{j \in \Lambda_i} k_{i,j}} \sum_{j \in \Lambda_i} y_j k_{i,j} : \tag{1}$$

where Λ_i is neighbourhood window of size $L \times L \times L$ voxels centred at voxel i. The weight $k_{i,j}$ can be a function of the spatial locations of voxels i and j, the intensities of the two voxels and/or the neighbourhood around them. In fact, many image filtering methods in the literature (e.g. Gaussian, bilateral and non-local means filtering methods) only differ in the choice of this kernel function [27].

Applying the above filter is equivalent to minimizing the following weighted least squares objective function [27]:

$$\hat{x_i} = \arg\min_{x_i} \quad \sum_{j \in \Lambda_i} (x_i - y_j)^2 k_{i,j} \tag{2}$$

The weights in the filtering operation, indicated as $k_{i,j}$ can be viewed as the parameters of the denoising method. In an ideal case, one would like to obtain the weights from the noise free ground truth image. Therefore, in practice, many denoising algorithms compute the weights from a pre-filtered image, or a so-called *guide image* to improve the estimate [27].

This is in particular very important for PET images with high levels of noise. For these images, a registered MR image from the same subject (resampled to the PET image space) has very low noise compared to the PET image and therefore can be used as the guide image to obtain these parameters.

Assuming that the guide image has a relatively low amount of noise compared to the PET image, the following simple yet effective kernel function is used in this work:

$$k_{i,j} = e^{-\frac{(v_i - v_j)^2}{2h^2}} \tag{3}$$

where v_i is the intensity of the i'th voxel in the *guide* image that corresponds to the spatial location of y_i in the PET image and h is the smoothing parameter of the filter. Note that, as opposed to patch-based filtering methods (such as non-local means) where the squared difference between patches need to be calculated, Eq.(3) only depends on the squared difference between *single* voxel intensities and hence is fast to compute. We refer to this method as guided kernel filtering (GKM), where $\mathcal{G}_i$ is a voxel-wise operation on voxel y_i defined using equation 1 and 3:

$$\hat{x_i} = \mathcal{G}_i(y_i) = \frac{1}{\sum_{j \in \Lambda_i} e^{-\frac{(v_i - v_j)^2}{2h^2}}} \sum_{j \in \Lambda_i} y_j e^{-\frac{(v_i - v_j)^2}{2h^2}} \tag{4}$$

B. Filtering in matrix notation

Let $\mathbf{K}$ be a symmetric positive semi-definite matrix of size $I \times I$. If voxel j is in the neighbourhood of voxel i identified by λ_i, then the value of $k_{i,j}$ corresponds to the weight in the GKM algorithm; otherwise $k_{i,j}$ is set to zero. Note that, since in practice the size of the neighbourhood is much smaller than the size of the image, the resulting kernel matrix

$\mathbf{K}$ is usually very sparse. Applying GKM on the image $\mathbf{y}$ is identical to multiplying the row-normalized kernel matrix by the noisy image [27]:

$$\hat{\mathbf{x}} = \begin{bmatrix} \mathcal{G}_1(y_1) \\ . \\ . \\ . \\ \mathcal{G}_I(y_I) \end{bmatrix} = \frac{\mathbf{Ky}}{\mathbf{K}\vec{\mathbf{1}}} = \mathbf{Wy}, \tag{5}$$

where $\vec{\mathbf{1}}$ is an all-one vector of size I.

We refer to this row-normalized kernel matrix as $\mathbf{W}$. Even though matrix $\mathbf{W}$ is very sparse, storing the matrix for a 3D image may not be practical. In fact for a 3D image of size $256 \times 256 \times 207$ voxels and for a neighbourhood size of $7 \times 7 \times 7$ voxels, the matrix can have more than 4.6×10^9 non-zero elements (i.e. $I \times L^3$). Therefore, instead of explicit construction of this matrix the image $\hat{\mathbf{x}}$ is estimated by applying Eq.(4) on each voxel of noisy image $\mathbf{y}$.

C. Re-parametrization

Re-parameterization of PET images within reconstruction have been used as a means of regularization [18, 20–22, 37, 42]. In re-parametrization, the denoised image $\hat{\mathbf{x}}$ is represented as a superposition of some basis vectors $\mathbf{A}_1$ to $\mathbf{A}_\mathbf{l}$:

$$\hat{\mathbf{x}} = \sum_{l=1}^{L} \theta_l \mathbf{A}_l = \mathbf{A}\boldsymbol{\theta} \tag{6}$$

where $\mathbf{A}$ is a matrix of size $I \times L$ in which the l'th column A_l is the $l'th$ basis vector. $\boldsymbol{\theta}$ is the coefficient vector in which each element θ_l is the coefficient for the l'th basis vector.

The choice of basis function can range from blobs [22], to sophisticated structural-based basis functions, e.g. patch-based dictionaries learned from MR data [37]. Row-normalized kernel matrices have also been used for re-parametrization of PET images within reconstruction [29, 42]. When using a row-normalized kernel matrix extracted from a guide image for re-parameterization, each column i (i.e. basis function i) indicates the similarity of voxel i to other voxels in the guide image.

Once the basis matrix is calculated (or learned) from the guide image, the coefficient vector $\boldsymbol{\theta}$ is estimated by optimizing a pre-defined objective function. For reconstruction this

objective function is usually the log likelihood of the coefficient vector given the measurement data. For post-reconstruction denoising, the coefficient vector can be estimated by minimizing the representation error (i.e., the squared difference between the noisy image and the re-parameterized image).

D. Proposed Method 1: PET-MR Guided kernel re-parameterization

In this section, a novel method for denoising PET images using the subject's MR image, registered and resampled to the PET image space, is proposed. In this method, the signal in the denoised PET image is re-parameterized using *two sets* of basis functions, one obtained from the registered MR image and the other obtained from the PET image:

$$\hat{\mathbf{x}} = \mathbf{M}\boldsymbol{\alpha} + \mathbf{P}\boldsymbol{\beta} \tag{7}$$

where $\mathbf{M}$ is a basis matrix calculated from the MR image and $\mathbf{P}$ is the basis matrix calculated from the median-filtered PET image. $\boldsymbol{\alpha}$ and $\boldsymbol{\beta}$ are the coefficient vectors for these basis matrices respectively. A detailed description of how these basis matrices are obtained and how the coefficient vectors are estimated is provided in the following sections.

1. Basis formation

Before basis matrix formation, both the median-filtered PET image and the registered MR image are normalized by their maximum value so that each image contains values between 0 and 1. Once the images are normalized, the GKM formulation in Eq. (3) is used to construct two kernel matrices, one from the registered MR image and the other from the median-filtered PET image. The resulting matrices are then row-normalized to obtain $\mathbf{M}$ and $\mathbf{P}$ respectively. As mentioned before, $\boldsymbol{\alpha} \in \mathbb{R}^I$ and $\boldsymbol{\beta} \in \mathbb{R}^I$ are the coefficient vectors for these basis matrices. In the following section, an algorithm to estimate the coefficient vectors is presented. This re-parameterization framework is illustrated in Fig. 1.

2. Problem formulation

The coefficients for basis matrices $\mathbf{M}$ and $\mathbf{P}$ can be estimated using a least-squares objective function. Note that the median-filtered PET image does not contain detailed boundary

information due to low resolution (and high noise) in the PET image. Therefore, one would like the restored image to contain minimal signal represented by the PET basis matrix, i.e., only in regions where the PET image does not agree with the MR image (e.g., a lesion in PET not present in the MR). One way to control the contribution of the PET basis matrix in the final restored image is to impose a sparsity penalty on the coefficients of this matrix. This is done by adding an l_1 norm penalty to the least squares objective:

$$\arg\min_{\boldsymbol{\alpha},\boldsymbol{\beta}} \quad \|\mathbf{y} - (\mathbf{M}\boldsymbol{\alpha} + \mathbf{P}\boldsymbol{\beta})\|_2^2 + \lambda \|\boldsymbol{\beta}\|_1 \tag{8}$$

where λ is a hyper parameter that controls the sparsity of $\boldsymbol{\beta}$.

3. Algorithm

The above optimization problem can be solved in an alternating manner by fixing $\boldsymbol{\beta}$ and solving for $\boldsymbol{\alpha}$ and then fixing for $\boldsymbol{\alpha}$ and solving for $\boldsymbol{\beta}$ iteratively.

4. Subproblem 1:solving for $\boldsymbol{\alpha}$

Fixing β leads to the following problem:

$$\arg\min_{\boldsymbol{\alpha}} \quad \|\mathbf{y} - (\mathbf{M}\boldsymbol{\alpha} + \mathbf{P}\boldsymbol{\beta})\|_2^2 \tag{9}$$

Considering that $\mathbf{M}\vec{\mathbf{1}} = \vec{\mathbf{1}}$, this least squares problem that can be solved using, for example, the simultaneous algebraic reconstruction technique (SART) [1]. The SART update rule for the above objective function is as follows:

$$\boldsymbol{\alpha}^{k+1} = \boldsymbol{\alpha}^k + \frac{\mathbf{M}^T \frac{((\mathbf{y}-\mathbf{P}\boldsymbol{\beta})-\mathbf{M}\boldsymbol{\alpha}^k)}{\mathbf{M}\vec{\mathbf{1}}}}{\mathbf{M}^T\vec{\mathbf{1}}} \tag{10}$$

5. Subproblem 2: solving for $\boldsymbol{\beta}$

Fixing $\boldsymbol{\alpha}$ and solving for $\boldsymbol{\beta}$ leads to a large-scale lasso problem. We use the fast iterative shrinkage-thresholding algorithm (FISTA) [5] to solve this problem. FISTA is shown in algorithm 1. The parameter c should be set to a value greater than the largest eigenvalue of $\mathbf{P}\mathbf{P}^T$ which is obtained using the power iteration method [13]. S_λ is the soft-thresholding operator defined as [11]:

$$S_\lambda(x) = \text{sign}(x)\ \max(|x| - \lambda, 0) \tag{11}$$

Algorithm 1: FISTA

Initialize: $t_0 = 1$; $\mathbf{z}_0 = \boldsymbol{\beta}_0$;

while *Not converged* **do**

$k = k + 1$

$\boldsymbol{\beta}^k = S_{\lambda/c}(\mathbf{z}^k + (1/c)\mathbf{P}^t((\mathbf{y} - \mathbf{M}\alpha) - \mathbf{P}\mathbf{z}^k))$

$t^{k+1} = \frac{1+\sqrt{1+4(t^k)^2}}{2}$

$\mathbf{z}^{k+1} = \boldsymbol{\beta}^k + \frac{t^k-1}{t^{k+1}}(\boldsymbol{\beta}^k - \boldsymbol{\beta}^{k-1})$

end

6. Implicit matrix-vector multiplication

As previously mentioned, computing the row-normalized kernel matrix $\mathbf{W}$ for a 3D image is highly demanding on memory. However, both SART and FISTA involve a multiplication of either this matrix or its transpose by a vector. In the following we show how multiplying $\mathbf{W}$ and $\mathbf{W}^T$ by an arbitrary vector $\boldsymbol{\theta}$ can be performed implicitly.

Let us define the operation $\mathcal{S}_i$ as the guided kernel sum (GKS) of the i'th voxel of image $\boldsymbol{\theta}$ using $\mathbf{K}$ as:

$$\mathcal{S}_i(\theta_i) = \sum_{j \in \Lambda_i} \theta_j k_{i,j} \tag{12}$$

This is similar to GKM but without normalization. Applying this operator on every voxel i in the image is equivalent to multiplying the kernel matrix by the image:

$$\begin{bmatrix} \mathcal{S}(\theta_1) \\ . \\ . \\ . \\ \mathcal{S}(\theta_J) \end{bmatrix} = \mathbf{K}\boldsymbol{\theta} \tag{13}$$

Using the GKS operator, basis matrix-vector multiplications can be performed implicitly as follows:

$$\mathbf{W}\boldsymbol{\theta} = \text{diag}^{-1}[\mathbf{K}\vec{\mathbf{1}}]\mathbf{K}\boldsymbol{\theta} = \frac{\mathbf{K}\boldsymbol{\theta}}{\mathbf{K}\vec{\mathbf{1}}} = \frac{\Big[\mathcal{S}_1(\theta_1) . \ . \ . \ \mathcal{S}_I(\theta_I)\Big]^T}{\Big[\mathcal{S}_1(1) . \ . \ . \ \mathcal{S}_I(1)\Big]^T} \tag{14}$$

This is equivalent to GKM. Now, considering that the kernel matrix is a symmetric matrix,

multiplication of the transpose of the basis matrix $\mathbf{W}$ by vector $\boldsymbol{\theta}$ can be written as:

$$\begin{aligned} \mathbf{W}^T\boldsymbol{\theta} = \quad & \mathbf{K}^T(\text{diag}^{-1}[\mathbf{K}\vec{\mathbf{1}}])^T\boldsymbol{\theta} = \\ \mathbf{K}\frac{\boldsymbol{\theta}}{\mathbf{K}\vec{\mathbf{1}}} = & \left[\mathcal{S}_1(\frac{\theta_1}{\mathcal{S}_1(1)}). \ . \ . \ \mathcal{S}_I(\frac{\theta_I}{\mathcal{S}_I(1)})\right]^T \end{aligned} \tag{15}$$

Here, the image is first normalized by $\left[\mathcal{S}_1(1). \ . \ . \ \mathcal{S}_I(1)\right]^T$ and then GKS is applied to the normalized image.

E. Proposed Method 2: PET-MR GKM with twicing

In this section, a very fast and simple alternative approach for denoising using weights obtained from the registered MR and median-filtered PET images is presented.

1. Twicing

The idea of twicing was first proposed by Tukey in the 1970s to improve the estimate in denoising algorithms [40]. In this method, the residual image (obtained as the difference between the original image and the estimated denoised image) is denoised and then added to estimated image:

$$\begin{aligned} \mathbf{r} &= \mathbf{y} - \text{filter}(\mathbf{y}) \\ \hat{\mathbf{x}} &= \text{filter}(\mathbf{y}) + \text{filter}(\mathbf{r}) \end{aligned} \tag{16}$$

If the residual contains some signal, denoising the residual helps to remove the noise and to recover that signal, and hence adding this filtered residual to the denoised image may improve the estimate. In principle, this process can be carried out for more than one iteration. Increasing the number of iterations will increase the noise in the resulting image.

2. Algorithm for Method 2

The rationale behind Method 2 is very similar to Method 1: in order to improve the boundary information in the restored image, we would like the parameters of GKM, i.e., the elements of $\mathbf{K}$, to be estimated from a noise-free image with detailed anatomical information. Hence using the MR image as the guide image in GKM seems very appealing.

However, since the kernel is obtained from the MR image, it may also remove some of the underlying signal in regions where PET and MR do not agree, e.g. a lesion in the PET that is not present in MR. This is where twicing plays an important role. The residual image contains some of the underlying signal specific to PET as well as noise. Denoising the residual using weights obtained from a median-filtered PET image helps to remove the noise from the residual, hence adding this denoised residual can recover part of the lost PET signal.

$$\begin{aligned} &\text{Step 1 :} && \hat{x}_i^{\mathrm{MR}} = \mathcal{G}_i^{\mathrm{MR}}(y_i) \\ &\text{Step 2 :} && \hat{x}_i^{\mathrm{Final}} = \hat{x}_i^{\mathrm{MR}} + \mathcal{G}_i^{\mathrm{PET}}(y_i - \hat{x}_i^{\mathrm{MR}}) \end{aligned} \tag{17}$$

$\mathcal{G}_i^{MR}$ and $\mathcal{G}_i^{PET}$ are defined by the GKM operator given in Eq. (4), in which the $k_{i,j}$ elements are obtained from the registered MR and the median-filtered PET image respectively. This method is illustrated in Fig.2.

Note that, similar to the proposed Method 1, before applying the GKM, both the median-filtered PET image and the registered MR image are normalized by their maximum intensity. Normalization brings both the median-filtered PET image and the MR image to be in a range between 0 and 1. This way the smoothing parameter of the kernel h can be chosen irrespective of the intensity range in the guide image. This enables us to use the same value of h for both the median filtered PET and the MR image.

F. Combination with PVE correction

In addition to noise, PVE in PET images is another very important source of error in PET quantification. When the point spread function (PSF) associated with PVE is known, deblurring algorithms can be used to improve the resolution of the PET image.

One issue with many iterative deblurring algorithms is that the ill-conditioned nature of deblurring leads to noise amplification in the resulting image[26, 38]. However, both of the proposed methods are able to remove a high amount of noise in the image. Therefore, applying these methods after deblurring can effectively reduce the normally encountered noise amplifications while still improving the boundary information.

1. Deblurring

For PVE correction, the Richardson-Lucy deblurring algorithm [23, 33] with the exact known stationary point spread function was applied to the reconstructed image to obtain the deblurred image $\mathbf{u}$. The update rule of Richardson-Lucy algorithm is shown below:

$$\mathbf{u}^{n+1} = \mathbf{u}^n \mathbf{C}^{\mathbf{T}} \frac{\mathbf{y}}{\mathbf{C}\mathbf{u}^n} \tag{18}$$

where $\mathbf{C}$ is the blurring matrix in which each column $\mathbf{c}_i$ indicates the PSF centred at voxel i.

III. EXPERIMENTS AND RESULTS

In this section the performance of the proposed methods is evaluated using both simulation and real data. The proposed methods are compared with Block-matching and 4D filtering (BM4D) method [24] and median filtering. BM4D is an extension of BM3D[10] denoising method to volumetric data. In BM3D, the image is first decomposed to patches and these patches are clustered based on similarity. This is followed by a 3-D collaborative Wiener filtering applied to each cluster. The resulting filtered patches are then aggregated to form the denoised image. In median filtering each voxel in the denoised image is simply the median of the neighbourhood around it.

A. Simulation

Simulated [^{18}F]fluorodeoxyglucose(FDG) PET images were used to evaluate the performance of the proposed methods. An MR image was obtained from the BrainWeb project [9] (`http:brainweb.bic.mni.mcgill.ca/brainweb`). In order to simulate HRRT PET images, the corresponding BrainWeb segmentation was re-sampled to the PET image space ($256 \times 256 \times 207$ isotropic voxels of $1.22mm \times 1.22mm \times 1.22mm$). Then radioactivity values from PET SORTEO [15] (`http://sorteo.cermep.fr/home.php`) for grey matter (GM) and white matter (WM) were used to generate a realistic [^{18}F]FDG radioactivity distribution at roughly MRI resolution.

Moreover, in order to evaluate the performance of the method in capturing information specific to the PET image, three lesions were added to the ground truth. Lesion 1 was added

in the WM with 50% activity increase relative to WM. Lesion 2 is embedded in the GM with 50% activity increase relative to the GM. Lesion 3 was embedded in GM with 70% activity reduction relative to GM. Lesion 1 is a sphere with a radius of 5 voxels located in the WM. Lesion 2 has a radius of 4 voxels and is located across the GM and WM boundary. Lesion 3 is located in the GM and follows the cortical boundaries. The volumes of lesions 1, 2 and 3 are 515, 389 and 297 voxels respectively.

Figure 3 shows the resulting ground truth PET along with the registered MR image. The resulting ground truth was forward projected using an HRRT scanner model to obtain a sinogram data with 256 radial bins, 288 azimuthal angles and 104 projection planes. Appropriate linear attenuation coefficient factors similar to [44] were also included in the forward projection. In order to simulate scatter and randoms, a smoothed sinogram with total activity equal to one quarter of the projected ground truth was added [37].

The proposed methods were evaluated at different noise levels, the resulting sinogram was scaled so that the expected number of counts will be equal to 50M (noise level 3),100M (noise level 2) and 150M (noise level 1). Note that these values are smaller than the number of counts normally acquired for a brain scan on an HRRT scanner. Poisson noise was then introduced to the resulting sinograms to generate 5 noisy realizations from each noise level. The exact known values for attenuation and scatter and random events were used for corrections within the reconstruction of the noisy measurement data. The OSEM (Ordered subset expectation maximization)[17] algorithm with 16 subsets and iterations varying from 1 to 10 were used to reconstruct the PET images.

In each iteration of the alternating optimization in proposed Method 1, both SART and FISTA were terminated when the relative change of the objective function was less than 0.02. Simulation analysis showed that running the alternating minimization loop for 10 iterations works well for different noise levels; more iterations lead to increased noise in the resulting images.

Both proposed methods were tested with neighbourhood sizes ranging from $5 \times 5 \times 5$ to $13 \times 13 \times 13$ voxels and the smoothing parameter h ranging 0.02 to 0.06. Method 1 was also tuned for sparsity parameter λ ranging from 0 to 0.02.

1. Combination with PVE correction

The process described in the simulation section was used to create an FDG ground truth. This time however, the ground truth was smoothed using a Gaussian kernel of size $7 \times 7 \times 7$ voxels and FWHM equal to 4mm. The resulting ground truth was then forward projected and Poisson noise was introduced to the resulting sinogram (trues + scatter and randoms) to generate 5 realizations. Scatter and random evens were also modelled with the same approximation mentioned as in the previous section. The expected number of counts in each of the resulting sinograms was 300×10^6. For PVE correction, 10 iterations of the Richardson-Lucy algorithm with the known PSF function (FWHM=4mm) was used. The proposed methods were then applied to the PVE corrected images. The methods were tested for the same range of parameters mentioned in the previous section.

B. Figures of merit

In order to assess the performance of the methods in reducing the noise, the ensemble-based normalized root mean squared error (n-RMSE) is obtained for each voxel within a ROI and across multiple realizations. The resulting voxel-based values are then averaged within the ROI.

$$\text{Mean voxel-based n-RMSE within ROI} = \frac{1}{|ROI|} \sum_{i \in \text{ROI}} \frac{\text{RMSE}_i}{x_i} \tag{19}$$

where $\text{RMSE}_i = \sqrt{\frac{\sum_{r=1}^{R} (\hat{x}_i^r - x_i)^2}{R}}$ is the root mean squared error of voxel i across R realizations.

Also, bias of the mean of the lesion, as well as the standard deviation of the mean of the lesions normalized by their true mean, computed across realizations are used to assess the performance of the proposed method. The known boundaries from the simulation are used to determine the lesions and the background regions.

Also, for quantitative evaluation of the proposed methods in regions where the functional activity does not agree with the anatomy, the mean contrast recovery coefficient (CRC) of the lesions specific to PET across multiple realizations was used. The CRC value of the lesion in one realization can be obtained as follows:

$$\text{CRC} = \frac{|\text{Mean anctivity in the lesion} - \text{Mean activity in the background}|}{|\text{known mean activity in the lesion} - \text{known mean activity in the background}|} \tag{20}$$

where the known mean activity is obtained from the ground truth.

For Method 1, there is trade-off between nRMSE and the contrast of the PET specific lesions. Therefore, to choose the optimum set of parameters, the following ratio was used:

$$\text{CRC to error ratio} = \frac{\overline{\text{CRC}_{\text{L1}}} \times \overline{\text{CRC}_{\text{L2}}} \times \overline{\text{CRC}_{\text{L3}}}}{\text{Mean n-RMSE within the brain}} \tag{21}$$

where $\overline{\text{CRC}_{\text{Li}}}$ indicates the mean CRC value across realizations for lesion Li.

The SNR of the restored image is another figure of merit used in our analysis:

$$\text{SNR}_{\hat{\mathbf{x}}^r} = \frac{\|\hat{\mathbf{x}}^r\|^2}{\|\hat{\mathbf{x}}^r - \mathbf{x}\|^2} \tag{22}$$

C. Results

Figure 4 shows the effect of smoothing parameter h and the neighbourhood length L on the mean voxel based n-RMSE within the brain for different noise levels. One can see that the 3 surfaces associated with 3 different noise levels follow a similar trend and hence the optimal set of parameters for obtaining minimum mean n-RMSE does not seem to be sensitive to the number of counts in the measurement data. Also, this figure shows that by decreasing the noise level the parameter surface becomes flatter. This indicates that for lower noise levels, the mean n-RMSE value is less sensitive to the choice of parameters.

Figure 5 shows axial views of the denoised image with increasing value of λ. Increasing sparsity of the PET-based coefficients by increasing the value of λ can lead to less noise in the resulting image. As indicated at the bottom of each image, this increase will lead to lower nRMSE value within the brain at the expense of a decrease in the mean CRC value.

Table II shows the parameters leading to maximum CRC to nRMSE ratio for both methods. For Method 1, higher noise levels require a slight increase in the sparsity parameter λ to achieve the optimal value.

Figures 6 and 7 show the performance of the proposed methods for noise level 2 (100 M) and noise level 3 (50 M) respectively. Noise level 1 (150 M) is not shown here; applying the methods on higher count levels leads to images with higher quality. The proposed methods are compared with OSEM with no post processing, median filtering and the BM4D algorithm [24] through different figures of merit. The plots show the proposed methods with parameters reported in Table II. For BM4D algorithm the MATLAB implementation by the authours (`https://www.cs.tut.fi/~foi/GCF-BM3D/`) with a Gaussian noise assumption and automatic noise standard deviation estimation was used.

Figure 6a shows the mean n-RMSE value within the brain as a function of number of iterations of OSEM. One can clearly see that the proposed methods provide a lower n-RMSE value compared to median filtering and the BM4D algorithm. Figure 6b-d show the bias versus normalized standard deviation of the mean activity for the 3 lesions. For the hot lesion in WM (lesion 1) and the hot lesion in the GM (lesion 2) proposed Method 1 delivers a smaller magnitude bias for any given standard deviation as compared to other methods. However, the bias of the cold lesion in the GM (lesion 3) has a larger magnitude after Method 2 than the other denoising methods.

Figure 7 shows the same figures of merit for noise level 2. Note that in Fig.7a, after 3 iterations of OSEM, Method 1 provides a lower mean n-RMSE value than Method 2.

Figure 8 shows a reconstructed image of one sample realization after 10 iterations of OSEM (column 2) and the resulting images after applying different methods for noise level 2 (top images) and noise level 3 (bottom images). Column 1 shows early terminated OSEM after 3 iterations.

One can see that for both noise levels the proposed methods provide less noisy images with improved cortical boundaries. Also, while the images denoised using Method 1 and Method 2 are very similar, the latter appears to be slightly noisier than the former, when looking at the white matter of images in Fig.8.

1. Sensitivity to mis-registration

In this section the sensitivity of the proposed methods to mis-registration between PET and MR is evaluated.

One simulated FDG image at noise level 1 (see table II) and after 10 iterations of OSEM, as described in section III, was used as the noisy PET image in this section. The corresponding MR image was rotated around z axis while keeping the PET image intact to simulate mis-registration between PET and MR images. The rotation angle was changed from 0 to 7 degrees and for each angle both proposed methods were applied to the noisy PET image.

Figure 9 shows the noisy PET, the rotated MR image as well as the result of application of Method 1 and Method 2 on the noisy image. Also, the PET-based components of the final denoised images for both Methods are illustrated. For Method 1, the PET-based component corresponds to $\mathbf{P}\boldsymbol{\beta}$ after convergence and for Method 2 the PET-based component is the

denoised residual in the second step.

In the case of perfect alignment between PET and MR (0 degree rotation), the PET-based component for both methods is mostly confined to the PET specific lesions, with other regions being near zero. As the misalignment increases, the PET-based component becomes more pronounced. This means that in the boundaries where the PET and MR become more inconsistent with misalignment, the median filtered PET image has more weight in guiding the noise reduction. Therefore, considering that the median filtered PET image is noisier than the T1-weighted MR image, for both methods, increasing the misalignment leads to a decrease in the SNR value.

In Fig.10, the mean squared error(MSE) within the brain and the CRC of the lesion in WM is plotted as a function of misalignment in degrees. These values are also plotted for OSEM with no denoising and after median filtering for reference. The MSE increases and then almost plateaus after 3 degrees rotation. Also note that while Method 1 provides a slightly lower MSE value, the CRC value in the Method 1 is lower than that of Method 2.

2. Combination with PVE correction

Figure 11 shows the mean n-RMSE within the brain for Method 2 when applied alone or after PVE correction as a function of the sparsity parameter and neighbourhood length. This figure indicates that the sensitivity of this figure of merit to these parameters is similar for both PVE-corrected and non-PVE corrected images. The parameters leading to minimum mean n-RMSE within the brain are shown in Table III.

Different figures of merit for noisy images with no post-processing and also with PVE correction using the Richardson-Lucy Method are shown in Fig.12. Method 2 is shown for parameters indicated in Table III. The results indicate that Method 2 when applied after PVE correction provides a measurable improvement in mean n-RMSE within the brain. The BM4D method, however, does not further improve the image when applied after PVE correction; this might be due to the changes in noise structure after PVE-correction. As shown in Fig. 12, PVE correction reduces the magnitude of the bias in all 3 lesions. Method 2 when applied after PVE-correction provides the lowest bias for all standard deviations for both the hot lesion in the GM and the hot lesion in the WM. However, the bias is higher for the cold lesion in GM compared to other denoising methods.

Figure 13 shows an example of a noisy image restored using Richardson-Lucy PVE correction algorithm with a combination of median filtering, BM4D and the proposed methods. One can see that noticeable increase in resolution can be obtained by applying proposed methods after Richardson-Lucy deblurring. Method 2 seems to provide more refined boundaries compared to Method 1 when applied on images with PVE.

D. Application to Real Data

List-mode data was obtained from injection of approximately 185 MBq [^{18}F]FDG to a healthy human participant scanned on a Siemens HRRT scanner. The OSEM with resolution modelling algorithm with 16 subsets and 10 iterations was used to reconstruct the image. The duration of the reconstructed frame was 40 minutes starting 20 minutes after injection. A total of about 340 million counts were recorded in this scan.

Figure 14 shows the resulting image in the transverse, coronal and sagittal views. Since resolution modelling was used within reconstruction the point spread function is small (comparable to the spatial resolution of 1.44 mm of the HRRT scanner when using 3D OSEM) [31] and hence PVE correction may not be necessary. The result of applying median filtering, BM4D and the proposed methods on the reconstructed image is also shown in this figure. One can clearly see that the proposed methods provide a less noisy image with improved cortical boundaries.

IV. DISCUSSION AND CONCLUSION

Two novel methods for denoising PET images were proposed. The proposed Method 1 (PET-MR guided kernel re-parameterization) relies on the re-parameterization of the PET image using row-normalized kernel matrices obtained from co-registered MR and median-filtered PET images. An algorithm to estimate the coefficients of these basis functions while imposing sparsity on coefficients for the PET-based basis functions was proposed.

In the proposed Method 2 (PET-MR GKM with twicing), we use the subjects MR for guided kernel filtering of the noisy image. The residual is then denoised using the median-filtered PET as the guide image. The denoised image and the denoised residual are then added together to obtain the final image. Due to its non-iterative nature, Method 2 is much

faster than Method 1.

While both Method 1 and Method 2 rely on PET and MR-based kernels, they use them differently. In Method 1 the sparsity parameter controls the weight of information between the MR and PET images to guide the denoising process. This parameter needs to be small to ensure that PET unique information does not suffer from strong blurring in the resulting image. In Method 2 however, since only the PET-based filter is applied to the residual, the method is not prone to severe blurring of the PET specific regions.

We have shown through simulation that the proposed methods are sensitive to misregistration between PET and T1-weighted MR images. Misalignment between PET and MR in our simulation led to noisier images. Also, a 6 degree misalignment around the z-axis can be considered as an example of a situation where there is noticeable inconsistency between PET and MR. Severe PET or MR unique abnormalities may have a similar effect. We have shown that these inconsistencies did not lead to serious artefacts in the resulting images. This is due to the fact that we are using both PET and MR in guiding our denoising process, therefore when MR information is inconsistent, both methods (given that the sparsity parameter for Method 1 is small) implicitly rely on PET to guide the denoising process in inconsistent regions.

Both methods can deal with high noise levels. Therefore, as also demonstrated in the simulation, it is suggested to run OSEM for more iterations than used in conventional practice in order to reduce the bias in the resulting image. We also show that the proposed methods, when applied after a conventional deblurring algorithm, can be considered as a voxel-based MR guided PVE-correction method. Therefore the proposed methods should be of great interest for voxel-based brain studies.

In this work two types of simulation were used to evaluate our methods, one without and one with PVE. We use simulation without PVE to explore the capability of the method in reducing the noise. However, real PET images also suffer from PVE. In presence of non-corrected PVE in the PET image, the consistency between PET and MR boundaries is reduced which will lead to less refined boundaries after restoration. Applying a simple deconvolution on the noisy image will highly correlate the noise, resulting in artefacts in the deblurred images. In this case, proposed Method 2 provides a lower overall error (mean nRMSE within the brain) than proposed Method 1.

One limitation of the proposed methods is that for a given set of parameters, the perfor-

mance of the methods in PET-specific regions depends on the size and the activity of that region. For example, for a very small PET specific lesion, a smaller neighbourhood size will lead to improved contrast in the lesion, at the expense of increased noise in the whole brain.

One advantage of the proposed methods compared to many other MR guided PVE correction methods in the literature is that both proposed methods can work without the need for segmentation of the MR image, which is an important source of error in PVE correction [15].

Note that in proposed Method 1, by including the forward model in the least squares objective function, this method can easily be extended to a reconstruction algorithm in which coefficients for the basis functions are estimated from the PET measured data. The proposed denoising framework can be used for denoising any functional modality using corresponding anatomical images, e.g. CT for SPECT and PET, T1-weighted MR for fMRI. Furthermore, images of other radiotracers with higher image quality could potentially also be used to guide the denoising process, similarly to what was proposed for reconstruction by Ellis et al[12].

This work only evaluated the use of the proposed methods on a simulated FDG brain image and one real FDG dataset. Further application and analysis of the proposed methods on more real data is needed to ensure their applicability to other PET radiotracers as well as to other applications e.g. whole body PET or preclinical PET where the method might be more sensitive to PET-MRI registration issues.

ACKNOWLEDGMENT

The authors would like to acknowledge Dr Caroline Paquette for providing the real [^{18}F]FDG data and the T1-weighted MR data.

This study was funded in part by the Canadian Institute of Health Research (CIHR MOP-111169), les Fonds de Research Sant Qubec Pfizer Innovation fund, National Science and Engineering Research Council of Canada (NSERC 4140438 - 2012), the EPSRC (EP/M020142/1) and the Wellcome EPSRC Centre for Medical Engineering at Kings College London (WT 203148/Z/16/Z). We also wish to thank the Famille Louise and Andr

Charron for financial support.

---

[1] A. H. Andersen and A. C. Kak. Simultaneous algebraic reconstruction technique (sart): a superior implementation of the art algorithm. *Ultrasonic imaging*, 6(1):81–94, 1984.

[2] B. A. Ardekani, M. Braun, B. F. Hutton, I. Kanno, and H. Iida. Minimum cross-entropy reconstruction of PET images using prior anatomical information. *Physics in Medicine and Biology*, 41(11):2497, 1996.

[3] H. H. Barrett, D. W. Wilson, and B. M. Tsui. Noise properties of the EM algorithm. I. Theory. *Physics in medicine and biology*, 39(5):833, 1994.

[4] F. Bataille, C. Comtat, S. Jan, F. Sureau, and R. Trebossen. Brain PET partial-volume compensation using blurred anatomical labels. *IEEE Transactions on Nuclear Science*, 54(5):1606–1615, 2007.

[5] A. Beck and M. Teboulle. A fast iterative shrinkage-thresholding algorithm for linear inverse problems. *SIAM journal on imaging sciences*, 2(1):183–202, 2009.

[6] N. Boussion, C. Cheze Le Rest, M. Hatt, and D. Visvikis. Incorporation of wavelet-based denoising in iterative deconvolution for partial volume correction in whole-body PET imaging. *European journal of nuclear medicine and molecular imaging*, 36(7):1064–1075, 2009.

[7] T. Carlier, L. Ferrer, H. Necib, C. Bodet-Milin, C. Rousseau, and F. Kraeber-Bodéré. Clinical necr in 18f-fdg PET scans: optimization of injected activity and variable acquisition time. relationship with snr. *Physics in medicine and biology*, 59(21):6417, 2014.

[8] C. Chan, R. Fulton, D. D. Feng, and S. Meikle. Median non-local means filtering for low snr image denoising: Application to PET with anatomical knowledge. In *IEEE Nuclear Science Symposuim & Medical Imaging Conference*, pages 3613–3618. IEEE, 2010.

[9] C. A. Cocosco, V. Kollokian, R. K.-S. Kwan, G. B. Pike, and A. C. Evans. Brainweb: Online interface to a 3d MRI simulated brain database. In *NeuroImage*. Citeseer, 1997.

[10] K. Dabov, A. Foi, V. Katkovnik, and K. Egiazarian. Image denoising by sparse 3-d transform-domain collaborative filtering. *IEEE Transactions on image processing*, 16(8):2080–2095, 2007.

[11] I. Daubechies, M. Defrise, and C. De Mol. An iterative thresholding algorithm for linear inverse problems with a sparsity constraint. *arXiv preprint math/0307152*, 2003.

[12] S. Ellis, A. Mallia, C. J. McGinnity, G. J. R. Cook, and A. J. Reader. Multitracer guided

pet image reconstruction. *IEEE Transactions on Radiation and Plasma Medical Sciences*, 2(5):499–509, Sep. 2018.

[13] J. F. Epperson. *An introduction to numerical methods and analysis*. John Wiley & Sons, 2013.

[14] J. A. Fessler. Grouped coordinate descent algorithms for robust edge-preserving image restoration. In *Optical Science, Engineering and Instrumentation'97*, pages 184–194. International Society for Optics and Photonics, 1997.

[15] V. Frouin, C. Comtat, A. Reilhac, and M.-C. Grégoire. Correction of partial-volume effect for PET striatal imaging: fast implementation and study of robustness. *Journal of Nuclear Medicine*, 43(12):1715–1726, 2002.

[16] V. Frouin, C. Comtat, A. Reilhac, and M.-C. Grgoire. Correction of partial-volume effect for PET striatal imaging: Fast implementation and study of robustness. *Journal of Nuclear Medicine*, 43(12):1715–1726, 2002. cited By 99.

[17] H. M. Hudson and R. S. Larkin. Accelerated image reconstruction using ordered subsets of projection data. *IEEE transactions on medical imaging*, 13(4):601–609, 1994.

[18] F. Jacobs, S. Matej, and R. Lewitt. Image reconstruction techniques for PET. *Dep. Radiol., Univ. Pennsylvania, Philadelphia, Tech. Rep. MIPG245*, 1998.

[19] W. J. Jagust, D. Bandy, K. Chen, N. L. Foster, S. M. Landau, C. A. Mathis, J. C. Price, E. M. Reiman, D. Skovronsky, R. A. Koeppe, et al. The Alzheimer's disease neuroimaging initiative positron emission tomography core. *Alzheimer's & Dementia*, 6(3):221–229, 2010.

[20] J. Jiao, P. Markiewicz, N. Burgos, D. Atkinson, B. Hutton, S. Arridge, and S. Ourselin. Detail-preserving PET reconstruction with sparse image representation and anatomical priors. In *Information Processing in Medical Imaging*, pages 540–551. Springer, 2015.

[21] R. M. Lewitt. Multidimensional digital image representations using generalized kaiser–bessel window functions. *JOSA A*, 7(10):1834–1846, 1990.

[22] R. M. Lewitt. Alternatives to voxels for image representation in iterative reconstruction algorithms. *Physics in Medicine and Biology*, 37(3):705, 1992.

[23] L. B. Lucy. An iterative technique for the rectification of observed distributions. *The astronomical journal*, 79:745, 1974.

[24] M. Maggioni, V. Katkovnik, K. Egiazarian, and A. Foi. Nonlocal transform-domain filter for volumetric data denoising and reconstruction. *IEEE transactions on image processing*,

22(1):119–133, 2013.

[25] M. A. Mandelkern. Nuclear techniques for medical imaging: positron emission tomography. *Annual Review of Nuclear and Particle Science*, 45(1):205–254, 1995.

[26] M. Mignotte and J. Meunier. Three-dimensional blind deconvolution of spect images. *IEEE Transactions on Biomedical Engineering*, 47(2):274–280, 2000.

[27] P. Milanfar. A tour of modern image filtering: New insights and methods, both practical and theoretical. *IEEE Signal Processing Magazine*, 30(1):106–128, 2013.

[28] H. W. Müller-Gärtner, J. M. Links, J. L. Prince, R. N. Bryan, E. McVeigh, J. P. Leal, C. Davatzikos, and J. J. Frost. Measurement of radiotracer concentration in brain gray matter using positron emission tomography: MRI-based correction for partial volume effects. *Journal of Cerebral Blood Flow & Metabolism*, 12(4):571–583, 1992.

[29] P. Novosad and A. J. Reader. MR-guided dynamic PET reconstruction with the kernel method and spectral temporal basis functions. *Physics in medicine and biology*, 61(12):4624, 2016.

[30] J. Nuyts, J. Fessler, et al. A penalized-likelihood image reconstruction method for emission tomography, compared to postsmoothed maximum-likelihood with matched spatial resolution. *Medical Imaging, IEEE Transactions on*, 22(9):1042–1052, 2003.

[31] O. V. Olesen, M. Sibomana, S. H. Keller, F. Andersen, J. Jensen, S. Holm, C. Svarer, and L. Højgaard. Spatial resolution of the HRRT PET scanner using 3D-OSEM PSF reconstruction. In *Nuclear Science Symposium Conference Record (NSS/MIC), 2009 IEEE*, pages 3789–3790. IEEE, 2009.

[32] A. Rangarajan, T. Hsiao, and G. Gindi. A Bayesian joint mixture framework for the integration of anatomical information in functional image reconstruction. *Journal of Mathematical Imaging and Vision*, 12(3):199–217, 2000.

[33] W. H. Richardson. Bayesian-based iterative method of image restoration. *JOSA*, 62(1):55–59, 1972.

[34] O. Rousset, Y. Ma, and A. Evans. Correction for partial volume effects in PET: Principle and validation. *Journal of Nuclear Medicine*, 39(5):904–911, 1998. cited By 414.

[35] O. Rousset, A. Rahmim, A. Alavi, and H. Zaidi. Partial volume correction strategies in PET. *PET clinics*, 2(2):235–249, 2007.

[36] S. Strother, M. Casey, and E. Hoffman. Measuring PET scanner sensitivity: relating countrates to image signal-to-noise ratios using noise equivalents counts. *IEEE transactions on*

nuclear science, 37(2):783–788, 1990.

[37] M. S. Tahaei and A. J. Reader. Patch-based image reconstruction for PET using prior-image derived dictionaries. *Physics in Medicine and Biology*, 61(18):6833, 2016.

[38] B.-K. Teo, Y. Seo, S. L. Bacharach, J. A. Carrasquillo, S. K. Libutti, H. Shukla, B. H. Hasegawa, R. A. Hawkins, and B. L. Franc. Partial-volume correction in PET: validation of an iterative postreconstruction method with phantom and patient data. *Journal of Nuclear Medicine*, 48(5):802–810, 2007.

[39] K. Thielemans, C. Tsoumpas, S. Mustafovic, T. Beisel, P. Aguiar, N. Dikaios, and M. W. Jacobson. Stir: software for tomographic image reconstruction release 2. *Physics in medicine and biology*, 57(4):867, 2012.

[40] J. W. Tukey. Exploratory data analysis. 1977.

[41] F. E. Turkheimer, N. Boussion, A. N. Anderson, N. Pavese, P. Piccini, and D. Visvikis. PET image denoising using a synergistic multiresolution analysis of structural (MRI/CT) and functional datasets. *Journal of Nuclear Medicine*, 49(4):657–666, 2008.

[42] G. Wang and J. Qi. PET image reconstruction using kernel method. *IEEE transactions on medical imaging*, 34(1):61–71, 2015.

[43] J. Yan, J. C.-S. Lim, and D. W. Townsend. MRI-guided brain PET image filtering and partial volume correction. *Physics in medicine and biology*, 60(3):961, 2015.

[44] H. Zaidi, M.-L. Montandon, and A. Alavi. Advances in attenuation correction techniques in PET. *PET clinics*, 2(2):191–217, 2007.

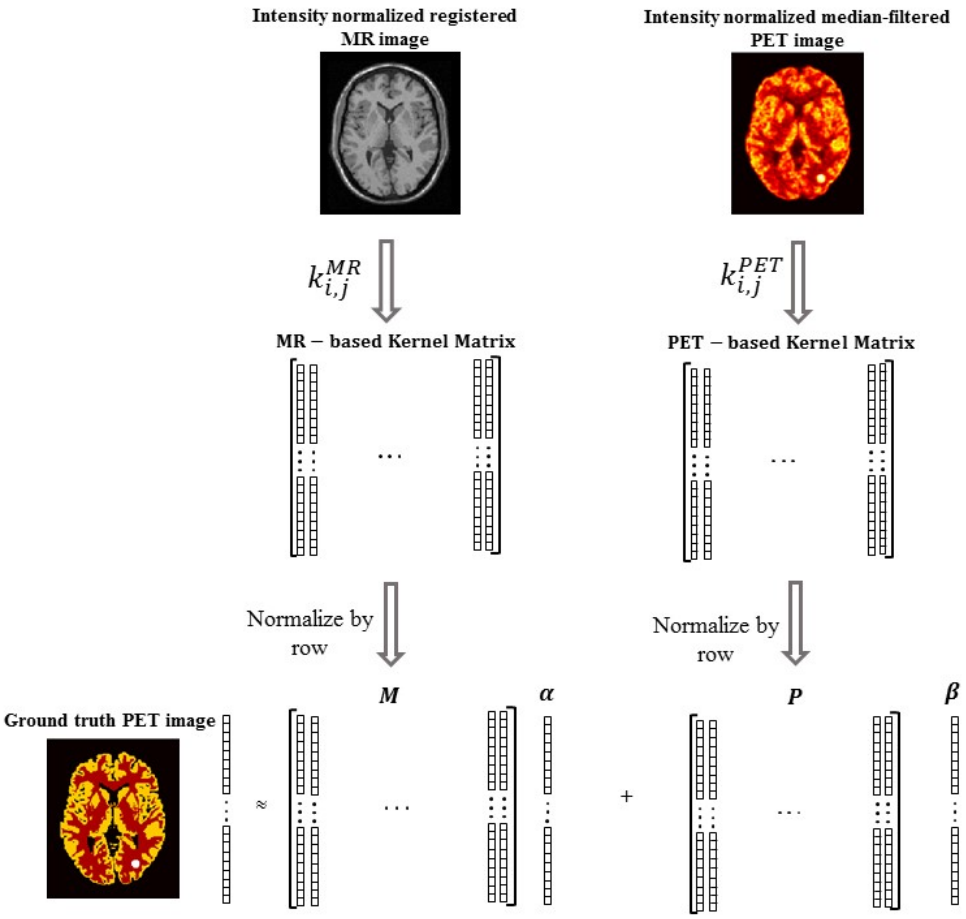

Figure 1. Illustration of the guided kernel re-parameterization in proposed Method 1. Two row-normalized intensity based kernel matrices are obtained, one from the normalized subject's registered MR image and the other from the normalized median-filtered PET image separately. These two matrices $\mathbf{M}$ and $\mathbf{P}$ are then used as basis matrices to re-parametrize the denoised PET image. In order to estimate the denoised image, the coefficient vectors for these basis matrices, namely α and β, have to be estimated by minimizing a sparsity-penalized least squares objective function.

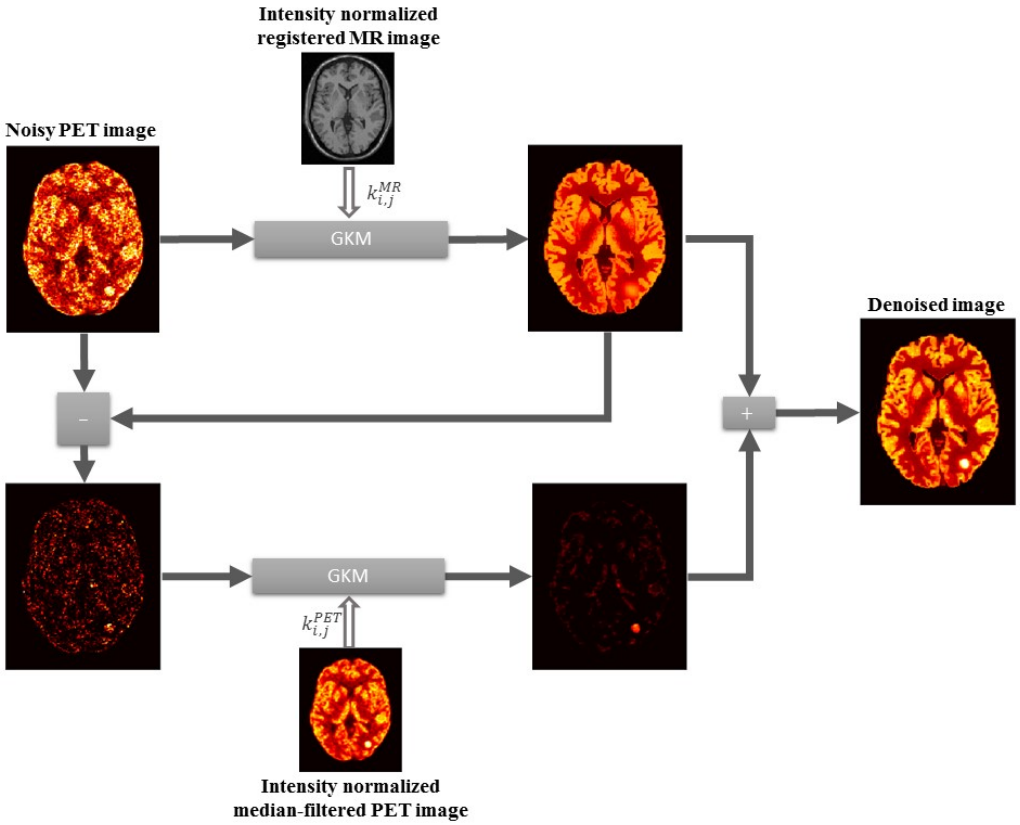

Figure 2. Illustration of proposed Method 2 (GKM with twicing): First the registered MR image is used as the guide image to denoise the PET image. The residual is then computed and denoised using a median-filtered PET image as the guide image. The denoised residual is then added to the denoised PET image.

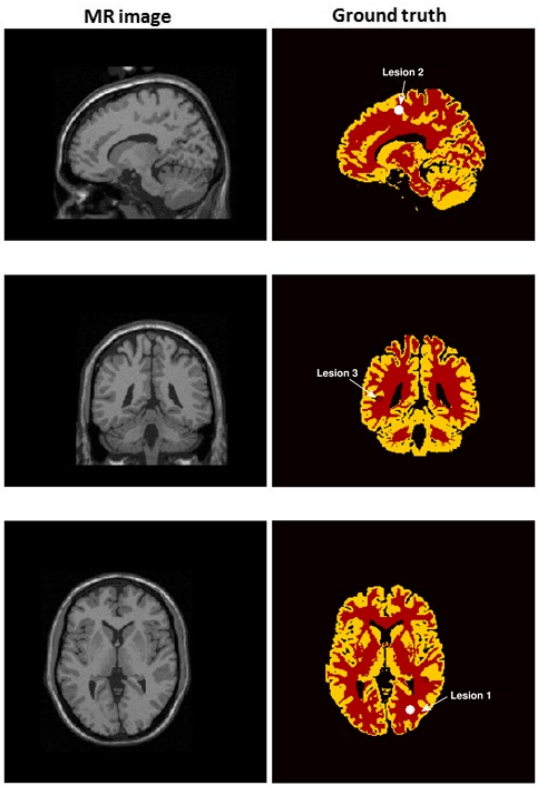

Figure 3. The simulated ground truth PET image and the corresponding registered T1-weighted MR image. The dimension of the image corresponds to an HRRT scanner field of view.

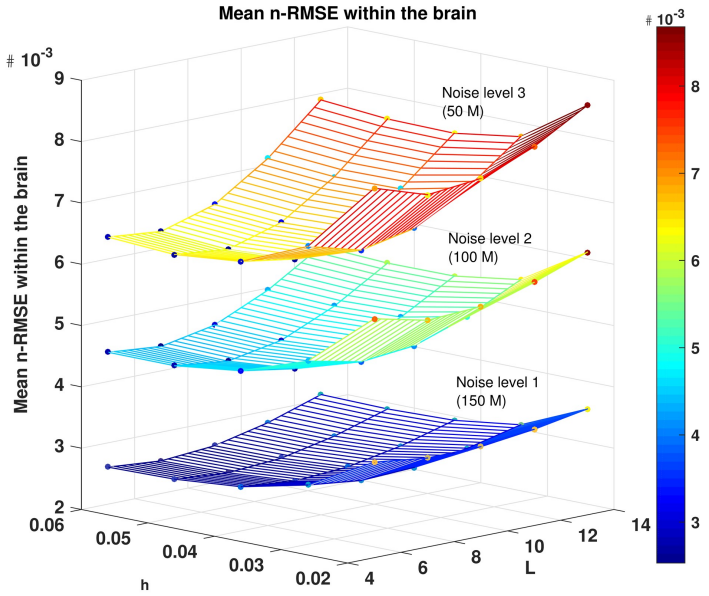

Figure 4. The mean n-RMSE within the brain as a function of smoothing parameter h and neighbourhood length L for the Method 2 shown for 3 different noise levels at their best iteration number (i.e., the OSEM iteration leading to minimum mean n-RMSE).

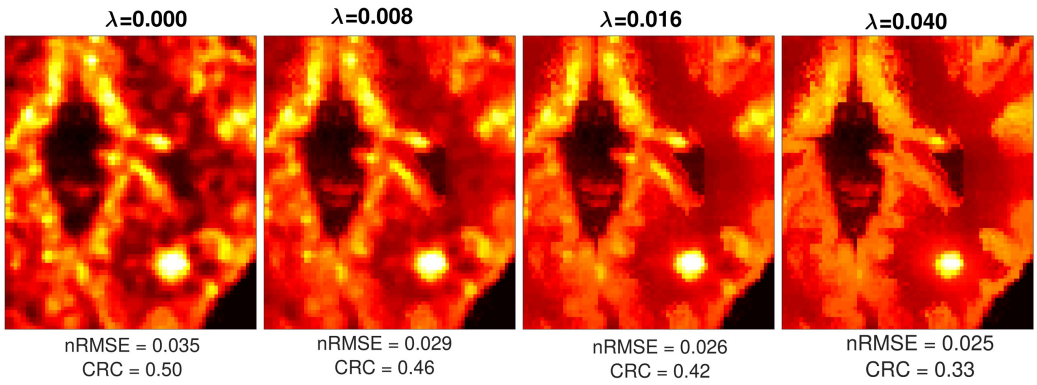

Figure 5. Transverse views of the simulation data showing the effect of increasing sparsity parameter λ of proposed Method 1 on image quality along with mean n-RMSE and mean CRC value of the lesion in WM for multiple realizations. By increasing the sparsity parameter the resulting images become less noisy; this leads to improvements in the nRMSE values within the brain at the expense of decrease in the CRC of the lesion in WM.

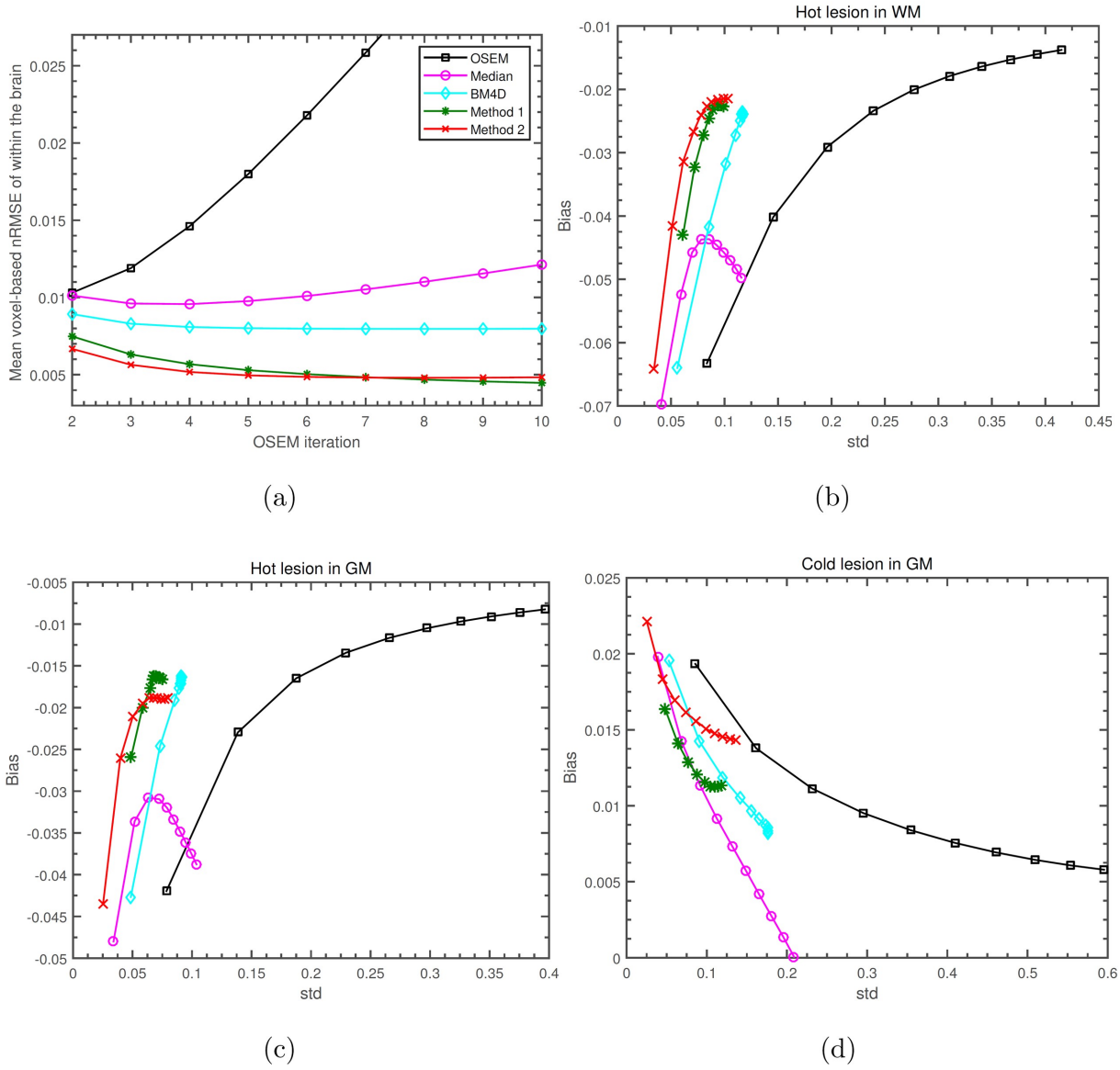

Figure 6. Different figures of merit for OSEM with no post-processing, median post-filtering, BM4D, Method 1 and Method 2 for noise level 2 (100 M counts). a) Mean n-RMSE within the brain as a function of iteration. Bias versus normalized standard deviation of the mean activity in the (b) hot lesion in the WM, (c) hot lesion in the GM and (d) cold lesion in the GM. Each data point corresponds to the figure of merit obtained from images that were reconstructed using a specific number of iterations of OSEM algorithm.

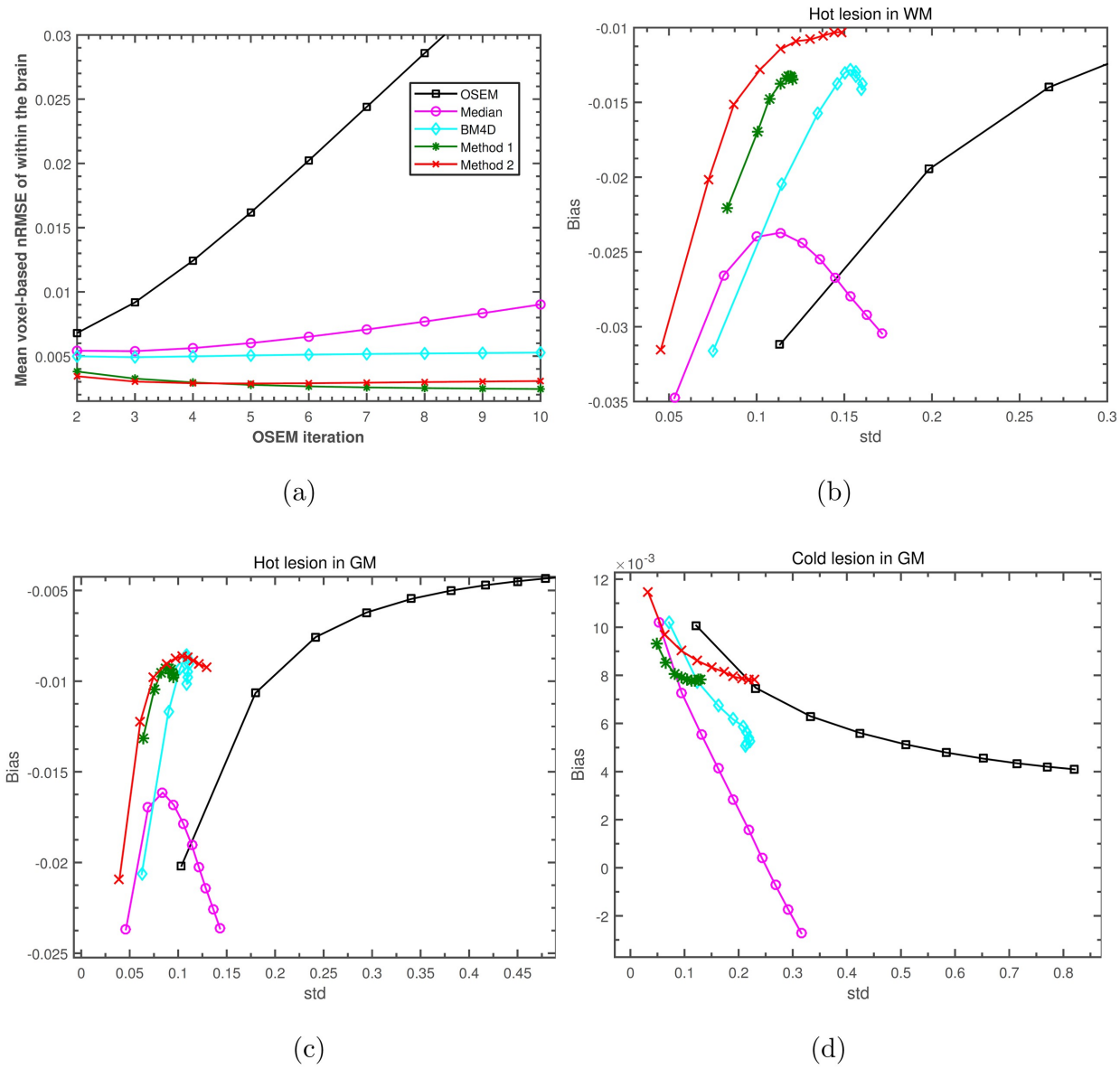

Figure 7. Different figures of merit for OSEM with no post-processing, median post-filtering, BM4D, Method 1 and Method 2 for noise level 3 (50 M counts). a) Mean n-RMSE within the brain as a function of iteration. Bias versus normalized standard deviation of the mean activity in the (b) hot lesion in the WM, (c) hot lesion in the GM and (d) cold lesion in the GM.

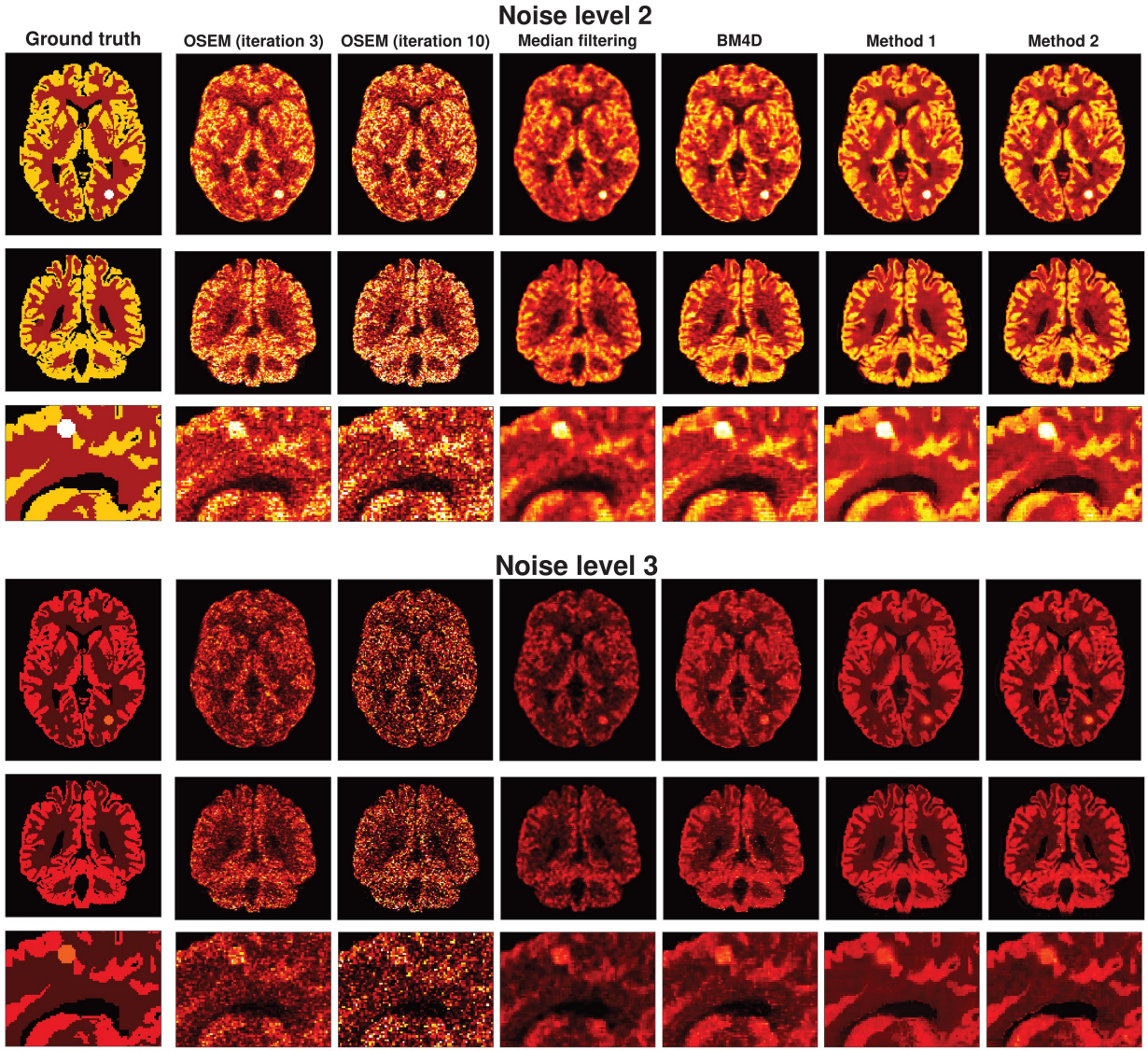

Figure 8. An example of our FDG simulation reconstructed using OSEM and then denoised using different methods. The images are shown for transverse, coronal and sagittal views. The ground truth image is show in Fig. 3. The axial and coronal views are cropped to focus on the brain. The sagittal view is zoomed for better visualization. All methods are shown with parameters indicated in Table II.

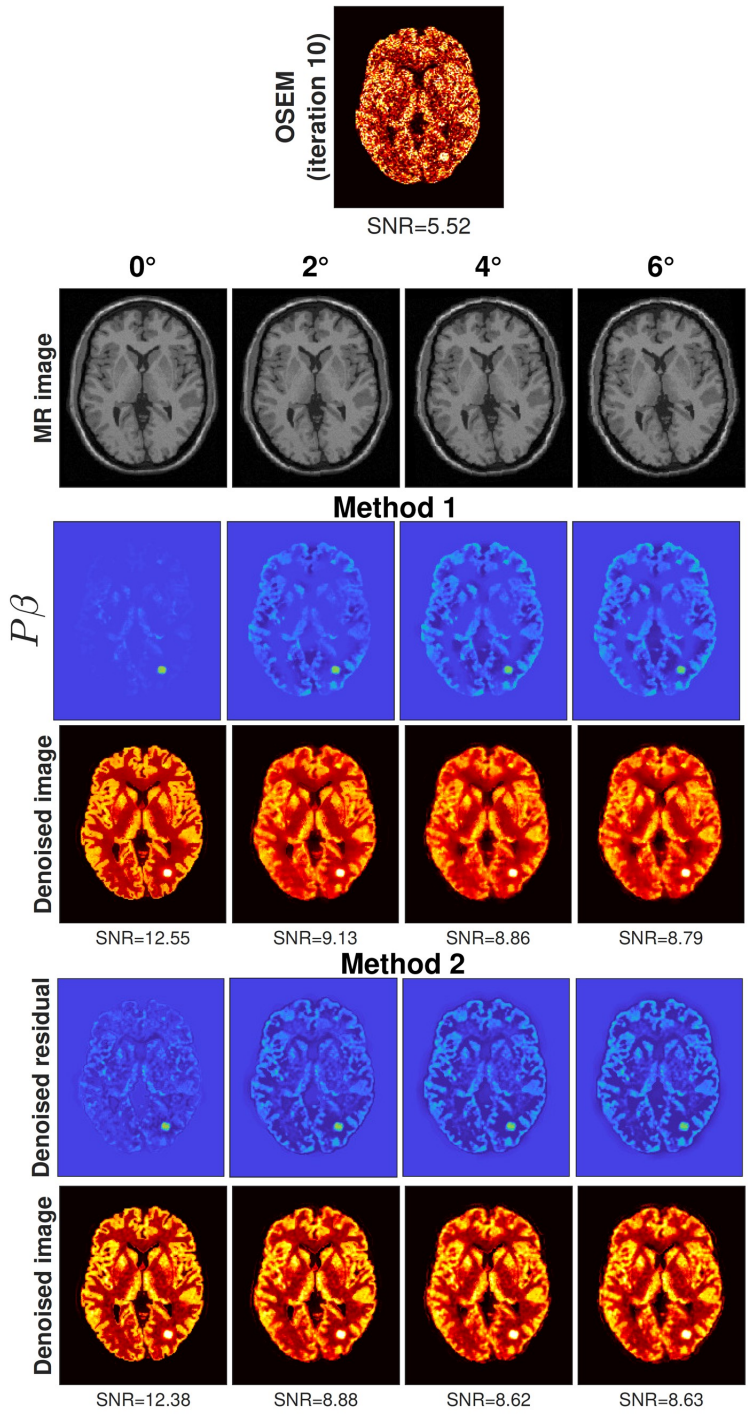

Figure 9. Example of applying Method 1 and 2 using misaligned MR images. The top row shows the noisy image (with Level 1 noise) on which the methods are applied. The MR image is rotated around z axis by 0, 2, 4 and 6 degrees. For each method the top row shows PET-based component of the final image. The SNR value is shown at the bottom of each image.

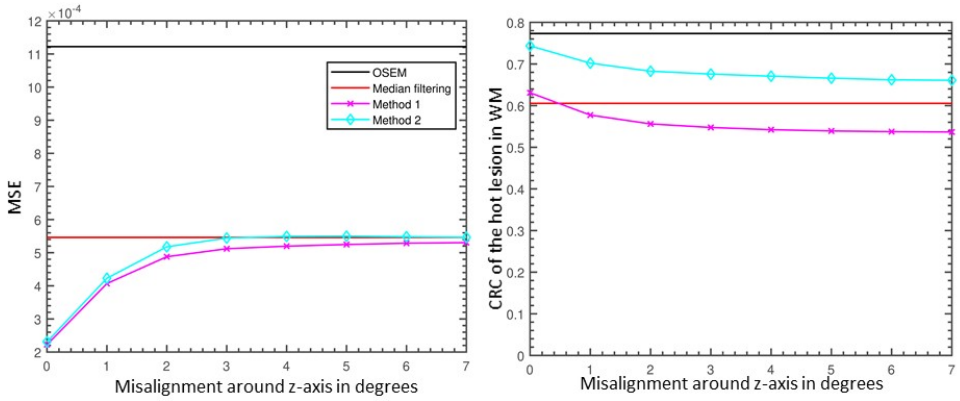

Figure 10. Left: mean squared error (MSE) within the brain as a function of rotational misalignment between PET and MR for Method 1 and Method 2. The MSE values for OSEM with no denoising and median filtering are also plotted for reference. Right: The CRC value of the lesion in white matter as as a function of rotational misalignment between PET and MR for Method 1 and Method 2.

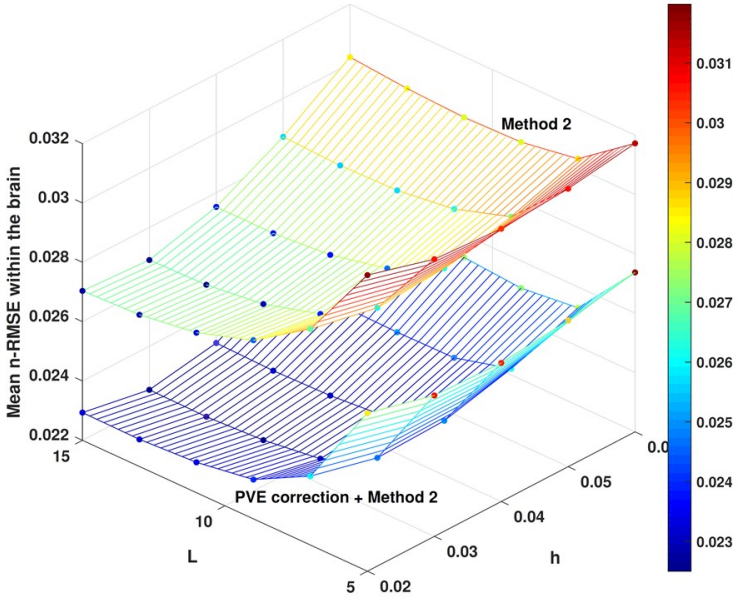

Figure 11. The normalized mean n-RMSE within the brain as a function of smoothing parameter h and neighbourhood length L for the Method 2 applied to images without PVE correction (Method 2) and applied to images after PVE correction (PVE correction + Method 2).

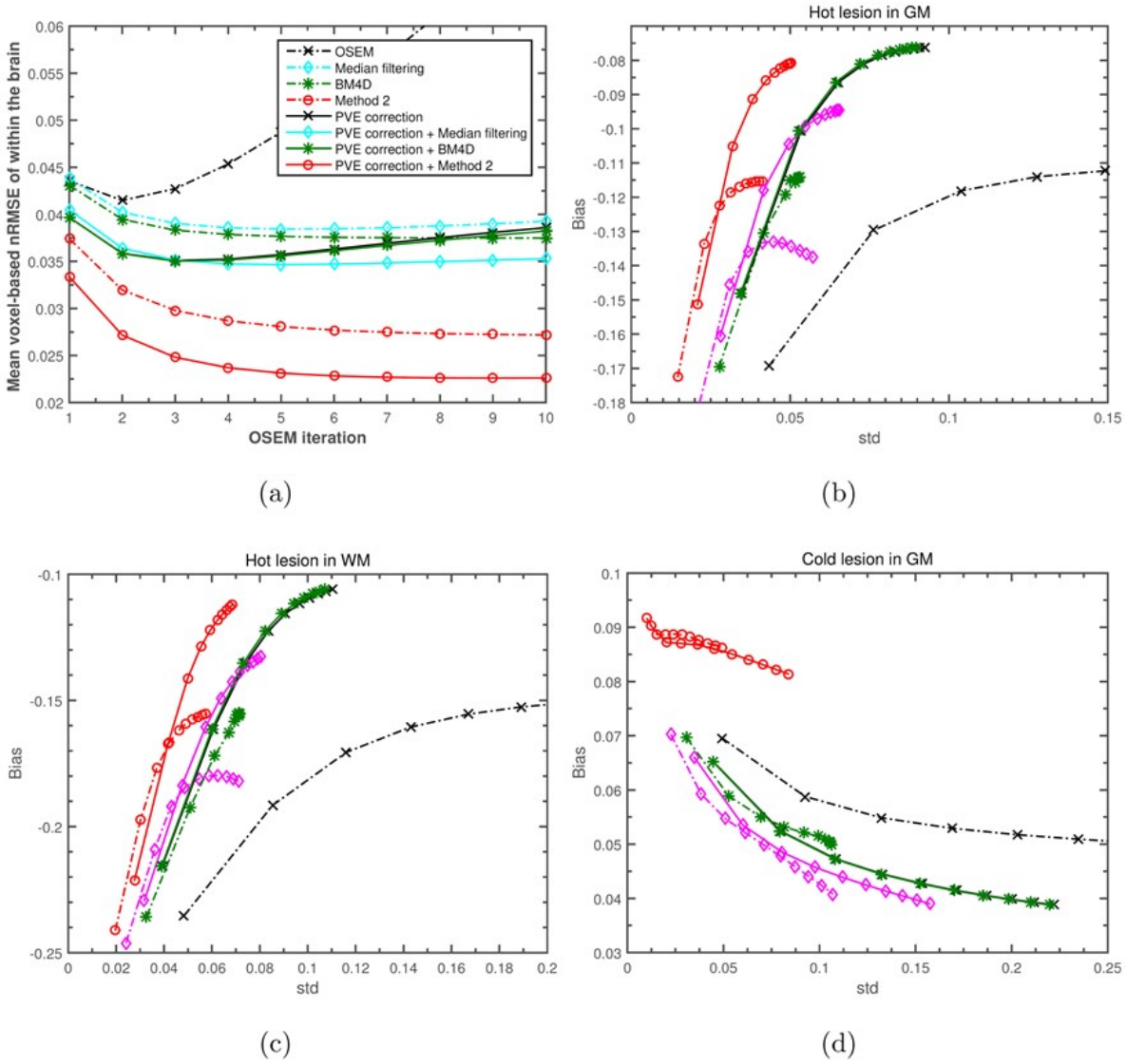

Figure 12. Different figures of merit for different methods when applied after OSEM reconstruction with no PVE correction as well as when PVE correction is applied after reconstruction. The parameters used for Method 2 are shown in Table III. a) Mean n-RMSE within the brain as a function of iteration. Bias versus normalized standard deviation of the mean activity in the (b) hot lesion in the WM, (c) hot lesion in the GM and (d) cold lesion in the GM. Note that applying BM4D after PVE correction provides almost no improvement over applying PVE correction alone in the resulting figures of merit.

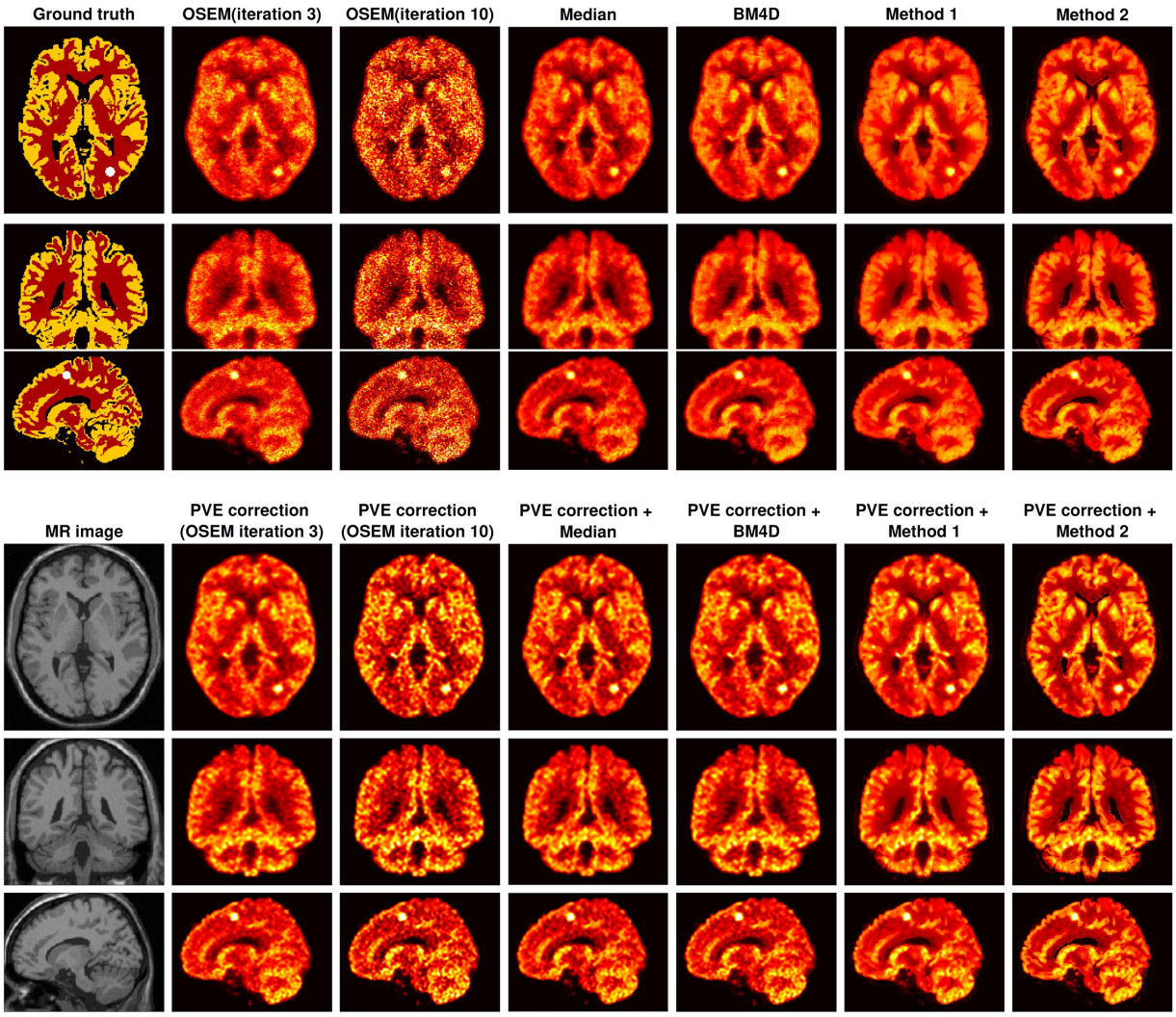

Figure 13. An example of a reconstructed FDG simulation. The images are cropped for better visualization. Top figure shows the noisy reconstructed image after 3 and 10 iterations of OSEM and when median filtering, BM4D and the proposed methods are is applied to the image after optimal number of iteration. The bottom figure shows when these methods are applied after PVE-correction.

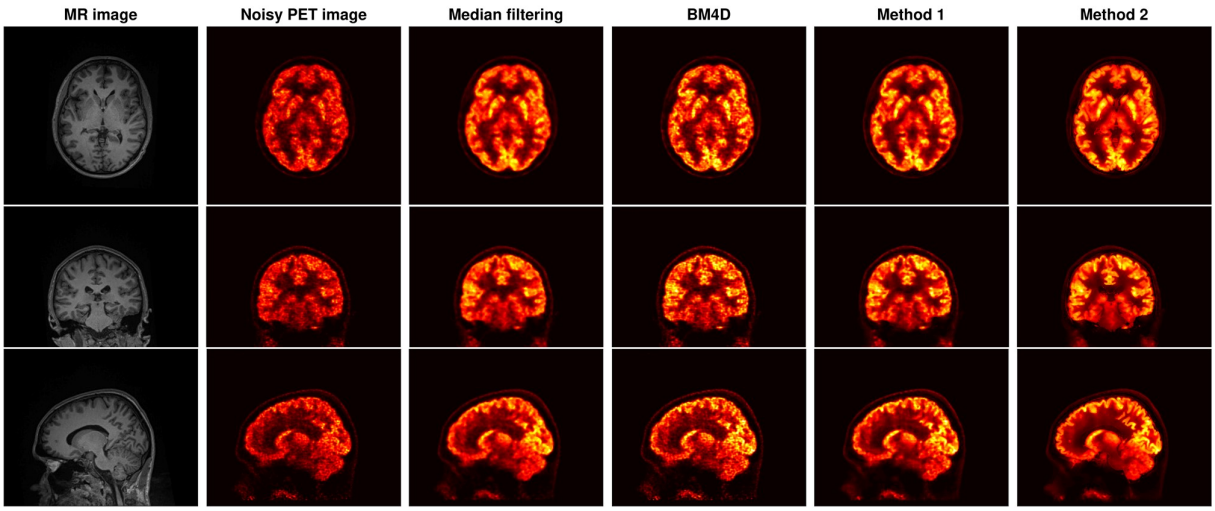

Figure 14. A real HRRT [^{18}F]FDG scan after 10 iterations of OSEM with 16 subsets as well as the denoised image after applying median filtering, BM4D and the proposed methods.

Table I. Summary of the meaning of some of the symbols and abbreviations used in the text

Symbol	Description
$\mathbf{x}$	True image
$\hat{\mathbf{x}}$	The estimated denoised image
$\mathbf{y}$	Noisy image
I	Number of voxels in $\mathbf{y}$
L	Neighbourhood lenght of the kernel
h	Smoothness parameter of the kernel
$\mathbf{K}$	Kernel matrix of size $I \times I$
$\mathbf{W}$	Normalized kernel matrix
$\mathbf{M}$	Normalized kernel extracted from the registered MR image
$\mathbf{P}$	Normalized kernel extracted from the median-filtered PET image
$\boldsymbol{\beta}$	Coefficient vector for P
$\boldsymbol{\alpha}$	Coefficient vector for M
λ	Sparsity parameter for Method 1
$\mathcal{G}_i$	Guided kernel means(GKM) applied to the i'th voxel in the image
$\mathcal{S}_i$	Guided kernel sum (GKS) applied on the i'th voxel in the image

Table II. Selected parameters for proposed methods

Method	Noise level (Counts)	OSEM iteration	**L**	**h**	**λ**	**n-RMSE**
Method 1	1 (150 M)	10	11	0.03	0.006	0.0022
	2 (100 M)	10	11	0.03	0.008	0.0040
	3 (50 M)	10	11	0.03	0.008	0.0059
Method 2	1 (150 M)	10	11	0.03	-	0.0026
	2 (100 M)	10	11	0.03	-	0.0044
	3 (50 M)	10	11	0.03	-	0.0063

Table III. Parameters leading to minimum mean n-RMSE within the brain

Method	OSEM iteration	**h**	**L**	**n-RMSE**
Method 2	10	13	0.03	0.0269
PVE correction + Method 2	9	13	0.03	0.0225